Non-contact measurement of partial gas pressure and distribution of elemental composition using energy-resolved neutron imaging

A. S. Tremsin, A. S. Losko, [iD] S. C. Vogel, et al.

View Online   Export Citation   CrossMark

ARTICLES YOU MAY BE INTERESTED IN

AIP Advances

Mathematical Physics Collection

READ NOW

Non-contact measurement of partial gas pressure and distribution of elemental composition using energy-resolved neutron imaging

A. S. Tremsin,[1,a] A. S. Losko,[2] S. C. Vogel,[2] D.D. Byler,[2] K. J. McClellan,[2] M. A. M. Bourke,[2] and J. V. Vallerga[1]

[1]*University of California at Berkeley, Berkeley, California 94720, USA*
[2]*Los Alamos National Laboratory, Los Alamos, New Mexico 87545, USA*

Neutron resonance absorption imaging is a non-destructive technique that can characterize the elemental composition of a sample by measuring nuclear resonances in the spectrum of a transmitted beam. Recent developments in pixelated time-of-flight imaging detectors coupled with pulsed neutron sources pose new opportunities for energy-resolved imaging. In this paper we demonstrate non-contact measurements of the partial pressure of xenon and krypton gases encapsulated in a steel pipe while simultaneously passing the neutron beam through high-Z materials. The configuration was chosen as a proof of principle demonstration of the potential to make non-destructive measurement of gas composition in nuclear fuel rods. The pressure measured from neutron transmission spectra ($\sim 739 \pm 98$ kPa and $\sim 751 \pm 154$ kPa for two Xe resonances) is in relatively good agreement with the pressure value of $\sim 758 \pm 21$ kPa measured by a pressure gauge. This type of imaging has been performed previously for solids with a spatial resolution of ~ 100 μm. In the present study it is demonstrated that the high penetration capability of epithermal neutrons enables quantitative mapping of gases encapsulate within high-Z materials such as steel, tungsten, urania and others. This technique may be beneficial for the non-destructive testing of bulk composition of objects (such as spent nuclear fuel assemblies and others) containing various elements opaque to other more conventional imaging techniques. The ability to image the gaseous substances concealed within solid materials also allows non-destructive leak testing of various containers and ultimately measurement of gas partial pressures with sub-mm spatial resolution. *© 2017 Author(s). All article content, except where otherwise noted, is licensed under a Creative Commons Attribution (CC BY) license (http://creativecommons.org/licenses/by/4.0/).* [http://dx.doi.org/10.1063/1.4975632]

I. INTRODUCTION

The penetrating capability of neutrons in most materials, coupled with their sensitivity to light atoms such as hydrogen, lithium and boron, make neutron radiography an attractive non-destructive option for the characterization of combinations of substances that include high-Z materials. Whereas the technique is frequently performed with a white spectrum using a thermal or cold neutron beam[1–3] the characterization options are greatly expanded by energy-resolved imaging[4–6] in which transmission spectra are measured for each pixel of the image. This allows spatially-resolved imaging of features related to microstructure variation such as texture and mosaicity,[7–10] residual strain[7,10–13] and phase distributions,[14] when thermal and cold neutrons are used. Studies that employ resonances appearing in the epithermal range of energies have been also reported for the investigation of elemental composition[15–21] and remote measurement of temperature.[22–24]

Energy-resolved measurements can be conducted at reactor sources using velocity selectors[25] and crystal monochromators[26] with energy resolutions (ΔE/E) of ~15% and ~3%, respectively.

---

[a]Author to whom correspondence should be addressed. Electronic mail: ast@ssl.berkeley.edu.

By contrast pulsed spallation neutron sources, which typically employ time of flight technique to resolve neutron energy, routinely offer energy resolution to sub-percent levels[4] and extend the spectral range to epithermal neutrons in excess of 10 keV.[15–24] In the region of ~1-10[5] eV many elements exhibit isotope-specific resonances that exist over narrow energy ranges specific to a particular isotope. Their existence results in sharp decreases in neutron transmission at discrete energies that indicate the presence of isotopes along the neutron path. For example the attenuation cross sections associated with resonances of xenon and krypton are shown in Fig 1. The depth of each resonance absorption dip depends on the cross-section and the amount of the contributing nuclei present in the neutron path quantified measurements are possible. At current facilities the measurable energy range is typically limited to less than ~10[4] eV by the width of the neutron pulse, the available flux, and by the level of background signal.[17–24] Thus current opportunities are best served for nuclides with resonances between ~0.1 eV and ~10 keV energies. Tabulated attenuation cross sections[27] exist for the majority of isotopes and can be used to evaluate experiment feasibility to resolve a particular element in a specific sample.

To date the majority of resonance absorption experiments were conducted with a single pixel device[17,22,23] or with a limited (~1-2 mm) spatial resolution.[15,16,20] However recent development of fast detection devices with 55 μm detector pixel size enables mapping the distribution of elements (including tomographic 3-dimensional imaging) and temperature in a solid sample with a ~100 μm resolution.

In this paper we demonstrate the use of neutron resonances to identify and measure the gas pressure of xenon and krypton gases in samples that also contain steel, gadolinium, urania and tungsten. By including knowledge of the volume of the gas canisters the method provides a direct determination of the partial pressure. The value of this demonstration derives from its potential application for non-destructive mapping of gaseous substances and measurement of their partial pressures in regions obscured by high-Z materials. These unique characterization capabilities offer potential characterization of fission gases in irradiated nuclear fuel rodlets, as well as remote leak testing of the rodlets that are sealed inside capsules for irradiation tests. At present experimental facilities quantified measurements are viable for gases that have resonance below ~1 keV. These
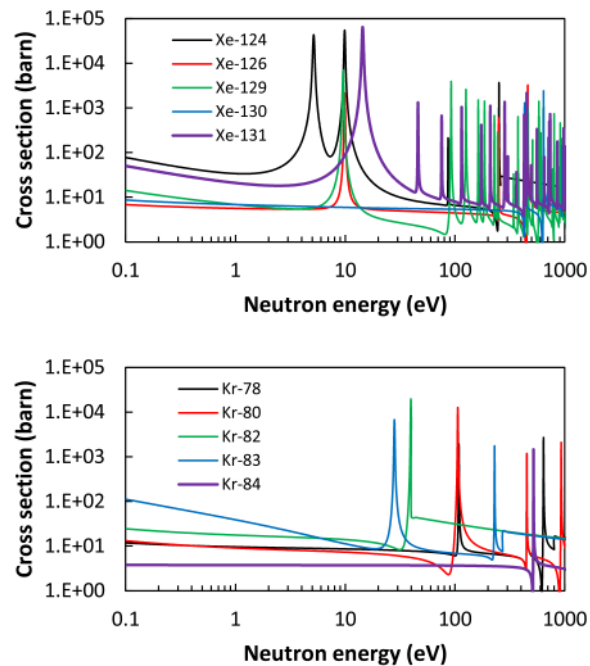

FIG. 1. Attenuation cross sections for Xe and Kr isotopes as a function of neutron energy.[27] The natural isotopic abundances are 0.095%, 0.089%, 26.4%, 4.07%, 21.2% for ^{124}Xe, ^{126}Xe, ^{129}Xe, ^{130}Xe, ^{131}Xe, and 0.35%, 2.25%, 11.6%, 11.5%, 57% for ^{78}Kr, ^{80}Kr, ^{82}Kr, ^{83}Kr, ^{84}Kr, respectively.

include Xe, Kr, UF_6 but not hydrogen or helium (while hydrogen and ^{3}He can still be imaged without their elemental specificity by thermal and cold neutrons due to their high attenuation cross section).

II. EXPERIMENTAL SETUP

To determine the energy of a neutron at a pulsed spallation source the time of flight (TOF) approach is used. The energy of a detected neutron is determined from its time of flight from creation to detection according to:

$$E_{kinetic} = \frac{p^2}{2m} = \frac{h^2}{2m\lambda^2} = \frac{mL^2}{2\,(T+\Delta T_0)^2} \tag{1}$$

where m is the mass of neutron, T is and ΔT_0 is the time delay of the trigger pulse relative to the time of spallation and L is the distance between the detector and the source of neutrons (typically the moderator), h is Plank's constant and λ is the neutron wavelength. At most spallation neutron sources the typical value of the flight path length L is between 10 and 25 m and for neutron energies from an eV to a keV the corresponding time of flight range is ~10 to ~1000 μs. The ability to record spatial and temporal information for every detected neutron in a pixelated detector is a crucial enabling technology. Recent developments of neutron detectors with ~55 μm spatial and 20 ns - 500 μs temporal resolution have enabled neutron resonance imaging with spatial resolution greater than ~100 μm.[19,28,29] Resonance imaging experiments have been previously performed with solid materials using resonances up to ~10 keV in energy[15–24] and we extend these studies to imaging gaseous substances.

The proof-of-principle experiments employed two separate tubular containers of natural xenon and krypton. They were mounted in three different configurations relative to steel rodlets containing urania fuel pellets with tungsten and gadolinium inclusions, as described in detail in Fig. 2. The geometry and dimensions of the urania-containing rods are consistent with light water reactor fuel. The gadolinium and tungsten inclusions existed for reasons unrelated to this study. Both xenon and krypton exhibit neutron resonances (~10^4 barn) in the region of 1 to 100eV (Fig. 1). The gases were contained in two separate stainless steel tubes (~12.7 mm outside Ø) each at an absolute pressure of ~110±3 psi (~758 kPa ± 21, ~7.5 ± 0.2 atm) measured by a pressure gauge.

Measurements were conducted at flightpath 5 at the pulsed neutron source at the Lujan Neutron Scattering Center at the Los Alamos National Laboratory.[30] The tubes of gas and rods containing the fuel pellets were installed in the direct beam in front of a detector as shown in Fig. 3. Neutron pulses at 20 Hz are generated by spallation of 800MeV proton pulses with a width of 270 ns base-to-base. After moderation by H_2O neutrons with a wide range of energies propagate along an 11.24 m flight
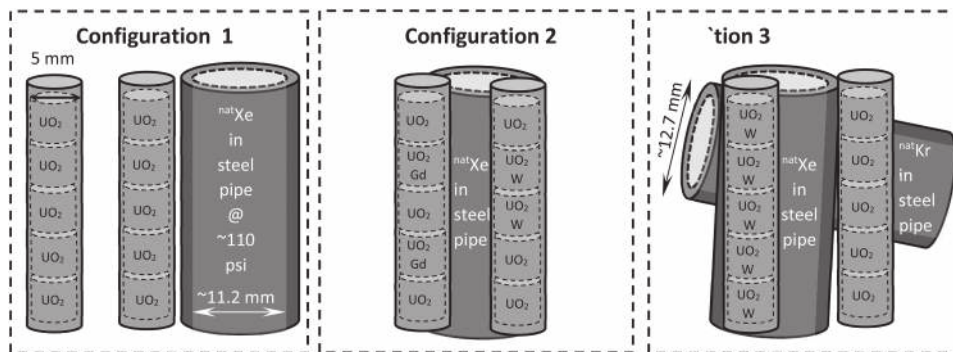

FIG. 2. Schematic diagram of sample assemblies used in the energy-resolved imaging experiments. Configuration 1 included two mockup nuclear fuel assemblies of ~5 mm depleted urania ($^{238}UO_2$) pellets mounted in steel cladding and a Xe gas contained in a steel pipe at absolute pressure of ~110 psi (758 kPa); Configuration 2 contained two fuel assemblies and Xe gas in a steel pipe. One fuel assembly contained ~1 mm wide Gd inclusions of various atomic concentration. The other assembly was the same as in configuration 3 with W wires; Configuration 3 had two fuel assemblies, and two steel pipes, with Xe and Kr gas at the same pressure. The urania pellets in one assembly had W wires of various diameters placed in the middle of the pellets.
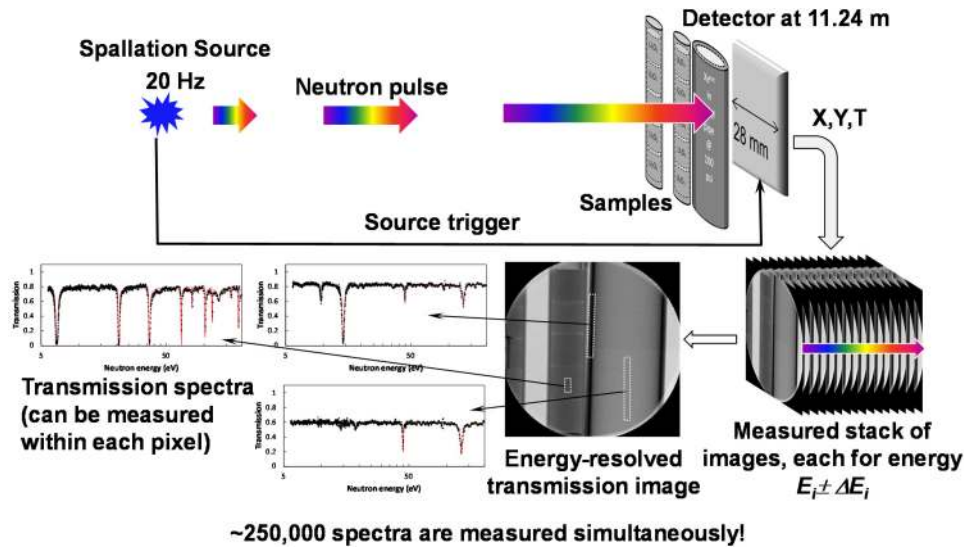
FIG. 3. Schematic of the experimental setup at the spallation neutron source at Los Alamos National Laboratory. The samples were mounted in front of a detector (512×512 pixels), interrogated by the neutron pulses at a 20 Hz frequency. 3000 spectral slices are recorded in each measurement providing individual transmission images corresponding to a neutron energy range $E_i \pm \Delta E_i$ with a spatial resolution of 55×55 μm^2.

path passing through the sample to the detector. The time of flight and position are recorded for each neutron detected in a 512×512 pixel (55 μm pixel width) detector. This provides simultaneous measurement of 262144 transmission spectra. The detector consisted of ^{10}B-doped neutron sensitive Microchannel Plates (MCPs), provided by Nova Scientific, Inc[31] and a quad Timepix readout. The capability of this detector to operate at counting rates exceeding 100 MHz and to detect more than 10^3 nearly simultaneous particles is a crucial enabling technology.[28,29] The intrinsic time resolution of the detector varies from ∼20 ns for keV neutrons, to ∼100 ns for eV neutrons and to ∼500 ns for meV neutrons. Open beam normalization (with no samples installed in front of the detector) was performed after background subtraction to eliminate the effects of beam spectrum and detector non-uniformities. Thus a neutron transmission spectrum $Tr(E)=(I(E)-Bgr)/(I_0(E)-Bgr)$ can be extracted for any sample region to a limit of 55×55 μm^2 pixel. The neutron flux and beam time constraints limit the number of neutrons acquired in the spectrum collected within a single pixel, making quantitative analysis to be very noisy. This problem was alleviated by integration spectra over multiple neighboring pixels during data analysis.

III. RESULTS AND DISCUSSION

Full spectrum transmission images for the three configurations are shown in Fig. 4. In this mode inclusions and voids within urania pellets can be visualized from changes in attenuation contrast, but cannot be explicitly identified. The gadolinium inclusions seen in configuration 2 exhibit a high thermal neutron absorption cross section and can be seen even for a lower atomic concentration. White spectrum images that do not require energy resolution can be acquired at any neutron source with sufficient flux and beam collimation. However, it is impossible to identify location of individual elements such as U, Xe, Kr, W or elements present in the steel pipe without a priori knowledge about the sample. For insight on the elemental and even isotopic makeup in such radiography, energy-resolved imaging extends what can be learnt from such measurements.

A. Calibration of neutron transmission spectra

The energy of each neutron registered by the detector was reconstructed from its time of flight according to Equation (1). Accurate values of the flight path length L and the delay of the trigger ΔT_0, as well as calibration of the beamline background are needed for the reconstruction of transmission
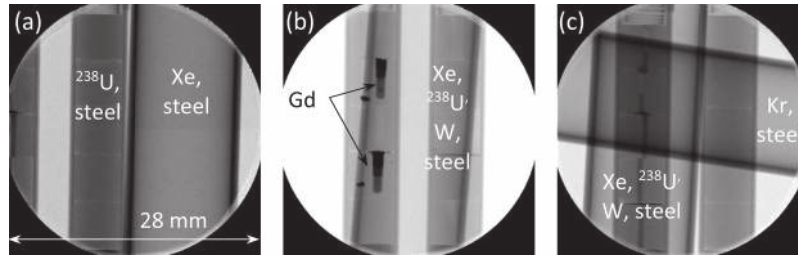
FIG. 4. Full spectrum (equivalent to white beam of flight path 5[30]) neutron radiographs of three sample configurations used in the experiments. The location of certain elements (inclusions in the samples) is specified in the images.

spectra. Calibration measurements with ^{238}U, Ta, Ag and Co foils were performed to calibrate the experimental setup. Opaque resonances (at energies for which less then few percent transmission is expected for the foil thicknesses) were used to assess the background as a function of neutron energy, as well as L and ΔT_0 parameters, as shown in Fig. 5.
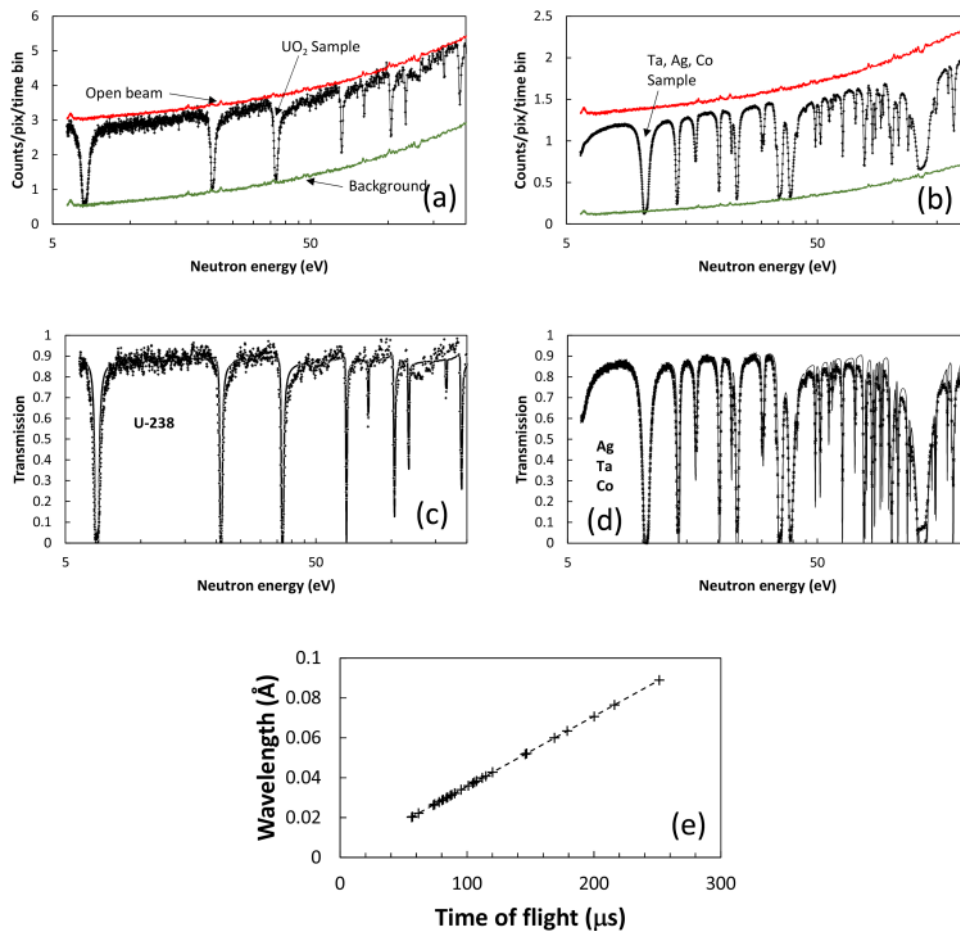

FIG. 5. Calibration of experimental parameters: background signal as a function of neutron energy, flight path L and trigger delay ΔT_0. (a), (b) – open beam spectra and spectra measured with foils of Ta (2.5 mm), Ag (0.19mm) and Co (0.1mm), all overlapped over urania (~5 mm cylinder). The background signal is calibrated using opaque resonances. (c), (d) measured (markers, background corrected) and calculated (solid lines) transmission spectra. (e) The time of flight values for opaque resonances (zero transmission) extracted from the measured data are plotted against tabulated resonance wavelengths extracted from ENDF database.[27] Linear fit into that curve is used for calibration of L and ΔT_0 parameters according to Equation (1).

For most neutron beamlines at spallation neutron sources (when no T_0 choppers are used) spectra registered in an open beam configuration exhibit an intensity increase towards higher energies and contain a larger fraction of the gamma photon and fast (>100 keV) neutron background signal. Choppers (that typically are used to mitigate background) are not fast enough to reduce the background without also curtailing the neutrons in the 1eV to 1 keV range that are used in resonance absorption imaging and therefore were not used in employed experiment. After subtraction of the background the resulting transmission curves shown in Figs. 5(c) and 5(d) were used for the extraction of parameters L and ΔT_0 from the linear dependence of neutron wavelength λ on the neutron time of flight, Equation (1). TOF values observed for the opaque resonances of known materials are plotted in Fig. 5(e) versus the tabulated resonance wavelengths (converted from energy) of these materials extracted from ENDF database.[27] The fitted straight line yields the parameter values L=11.241 m and ΔT_0=1.275 μs. The validity of our calibrations is confirmed by the good agreement between the measured data (shown by markers in Figs. 5(c) and 5(d)) and the theoretical transmission curves calculated from the known absorption cross section of ^{238}U, Ag, Ta and Co materials of a known thickness (shown in Figs. 5(c) and 5(d) by solid lines).

B. Reconstruction of the composition

1. Effective thickness of different elements

The energy-dependent transmission of a sample consisting of different materials can be calculated from the Beer-Lambert law:

$$Tr(E) = \frac{I(E)}{I_0(E)} = exp\left[-\sum_i N_i d_i \sum_j \sigma_{ij}(E) A_{ij}\right] \tag{2}$$

where N_i is the number of atoms of element i per unit volume, d_i is the effective thickness of that element integrated along the neutron path, $\sigma_{ij}(E)$ is the energy-dependent neutron attenuation cross section, and A_{ij} the abundance for the isotope j of element i, respectively. For solid materials the number of atoms per unit volume can be calculated from the known density of the material and atomic mass values m_{ij}:

$$N_i = \rho_i \frac{1}{\sum_j m_{ij} A_{ij}} \tag{3}$$

For gaseous materials the number of atoms of element i per unit volume can be approximated by an ideal gas equation:

$$N_i = \frac{s_i \sum_j P_{ij}}{kT} \tag{4}$$

where s_i is the number of atoms of element i per gas molecule, P_{ij} is the partial pressure of isotope j of gas containing element i, k is Boltzmann's constant and T is the absolute gas temperature. Separating attenuation by solid material from the attenuation of gaseous substances (steel, urania, tungsten attenuation from Xe and Kr gases in our experiments), the measured transmission can be expressed as multiplicative of two terms:

$$Tr(E) = Tr_{solid}(E) \times Tr_{gas}(E)$$
$$= \underbrace{exp\left[-\sum_i \frac{\rho_i d_i \sum_j \sigma_{ij}(E) A_{ij}}{\sum_j m_{ij} A_{ij}}\right]}_{solid\ materials} \times \underbrace{exp\left[-\frac{1}{kT}\sum_l s_l d_l \sum_j P_{lj}\sigma_{lj}(E) A_{lj}\right]}_{gaseous\ materials} \tag{5}$$

For quantitative characterization of reconstructed data multi-parameter fitting using theoretically calculated transmission spectra can be implemented. With sufficient statistics parameter reconstructions can be performed for individual detector pixels, as transmission spectra are measured within each of them. In practice the limited statistics acquired by a single pixel within a given measurement time necessitates integration of spectral data over multiple neighboring pixels. Post-experiment data binning provides flexibility in the analysis to select the smallest area consistent with the pre-requisite accuracy of the reconstructed parameters.

Quantification of solid materials using measured transmission spectra has been demonstrated for both resonance absorption[16,17,19,21,32] as well for the attenuation within a broad energy range, e.g. quantification of hydrogen content[33,34] in metals (enabled by the high incoherent scattering cross section of hydrogen nuclei). Here we demonstrate that gaseous partial pressure can also be reconstructed in situations when gases are concealed within high-Z materials. The analysis presented here allows reconstruction of either the partial pressure of the gas for a known volume occupied by that gas, or measurement of the gas volume for a known partial gas pressure [since gas pressure P and effective thickness d terms are multiplicative in Equation (5)]. In the present study we verified that either parameter could be determined from the measurements since both were known and could be tested in our reconstruction. It should be noted again that the feasibility of this technique relies on the existence of measureable resonances for a particular gas.

The possibility to reconstruct the volume occupied by gas (the gas "thickness" along the transmitted beam, to be more precise) is demonstrated in Fig. 6. Neutron transmission spectra obtained within the area of 0.28x17 mm^2 are shown for different positions within the tube of configuration 1
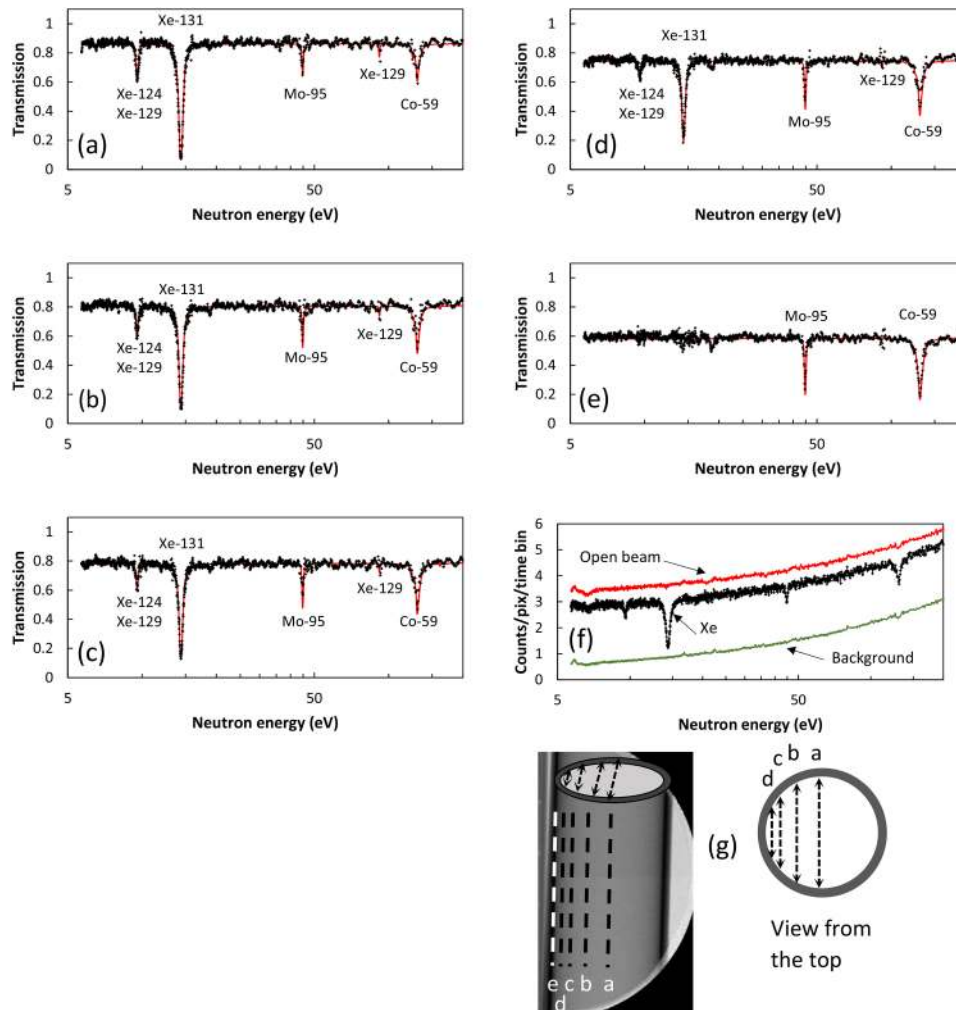

FIG. 6. Neutron transmission spectra extracted from the data set obtained with Xe-containing steel pipe of configuration 1. (a) – (e) Spectra measured within ~0.275x18 mm^2 areas (markers) and fitted transmission spectra (solid line) calculated from tabulated cross sections of these materials.[27] The locations of the corresponding areas are indicated in image (g) by dashed lines. (f) The raw transmission spectra measured within area (c) of the sample and in the same area of the detector with no samples placed in front of it ("open beam" spectra, used for normalization). The background spectra, calculated according to normalization described in Section III. A is also shown. (g) Full spectrum transmission image indicating the areas for which the transmission spectra (a)-(e) were extracted.

TABLE I. Fitted parameters: effective thickness (mm) occupied by specific elements.[a] All fitted values are with ~10-15% error bars. The expected values (obtained from sample geometry and known composition) are shown in parenthesis.

Fig. N	Xe	Fe	Mo	Co	^{238}U	W	Gd	Kr
6.a	11.2(11.2)	1.5(1.5)	0.026(0.026)	0.0028(0.0028)	· · ·	· · ·	· · ·	· · ·
6.b	9(9.05)	1.8(1.8)	0.031(0.0312)	0.0033(0.0034)	· · ·	· · ·	· · ·	· · ·
6.c	8(8.04)	2(1.99)	0.034(0.0344)	0.0037(0.0037)	· · ·	· · ·	· · ·	· · ·
6.d	6(5.04)	2.8(2.78)	0.048(0.0482)	0.0052(0.0052)	· · ·	· · ·	· · ·	· · ·
6.e	· · ·	5.5(5.49)	0.095(0.0952)	0.0103(0.0102)	· · ·	· · ·	· · ·	· · ·
7.b	· · ·	1.5(1.5)	0.026(0.026)	0.0028(0.0028)	· · ·	· · ·	· · ·	8(9)
9.b	· · ·	1.9(1.99)	0.0329(~0.344)	0.0034	1.8	· · ·	· · ·	· · ·
9.c	6(~5.5)	5.1(~5)	0.064(~0.07)	0.0085	4	0.03	· · ·	· · ·
9.d	11(~10.8)	1.9(~1.7)	0.0329(~0.03)	0.00355	· · ·	· · ·	· · ·	· · ·
9.e	6(~5.5)	5(~4.7)	0.054(~0.05)	0.0082	4	· · ·	0.1	· · ·

[a]Natural abundance (except for the ^{238}U isotope) and density (except for Xe and Kr gases) of solid materials is assumed. The known absolute pressure $P_{Xe} \approx P_{Kr} \approx 110$ psi (~758 kPa) were used in the fitting.

containing Xe gas, as explained by Fig. 6(g). The "thickness" of xenon as expressed by the depth of the xenon absorption can be seen to decrease from the center of the pipe towards the edge, while the thickness of steel increased, as reconstructed from transmission spectra via Mo and Co resonances, and non-resonant absorption by iron. The middle of the pipe [area (a)] has the largest effective thickness of Xe gas seen by the neutrons, which resulted in nearly opaque neutron resonance absorption at ~14.4 eV. The cross section (e) of Fig. 6 corresponds to the transmission of the steel pipe only. The corresponding measured spectra have a decreasing dip at the resonances of Xe gas in Fig. 6(a)–6(d) and decreasing overall transmission due to a larger absorption by Fe (with no resonances in that energy range) and increased absorption by Mo (~2.8 wt% as measured in our experiment) and Co contamination (<1 wt% in 316 stainless steel, from Ni alloying) in the steel of the pipe.

Multi-parameter fits of the effective thickness d_i for Fe, Co and Mo and d_l for Xe, derived using Equation (5) are shown as solid lines in figures 6.a through 6.e. Table I shows the fitted parameter values, which seem to agree with the expected values known from the steel composition, geometry of the pipe and the pressure of Xe and Kr gases measured by a gauge. Although Fe does not have resonances in the energy range accessible in this experiment, it still has non-negligible attenuation cross section and is taken into consideration during the analysis when the theoretical transmission spectra are calculated. Strictly speaking, a priori information on the existence of a steel pipe in our samples is necessary for the data analysis as the presence of Fe cannot be identified explicitly jus from the resonance spectra. All the experimental spectra shown in Fig. 6 were obtained after background subtraction and normalization by the open beam from the raw spectra shown in Fig. 6(f). The results demonstrate how thickness for both solid and gaseous materials can be extracted from the measured data, (providing there is sufficient resonance absorption by a particular material).

The same analysis can be performed for Kr sealed at ~110 psi (758 kPa) absolute pressure in a similar steel pipe. The spectrum extracted for a small area shown in Fig. 7 exhibits clearly
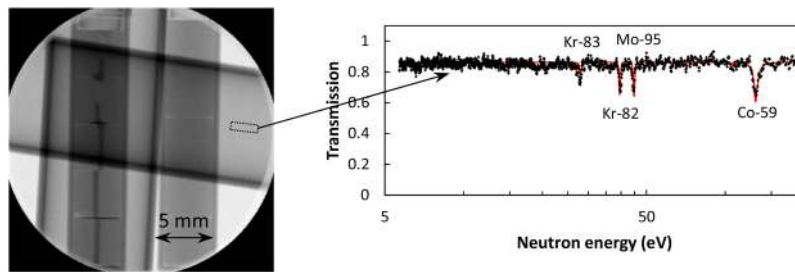

FIG. 7. Full spectrum (white beam) transmission image and the measured (markers) and fitted theoretical (solid line) spectra of Kr gas encapsulated in a steel pipe. Configuration 3 of sample assembly used in this experiment. The small rectangle indicated on the transmission image indicates the area for which the spectrum was extracted.

distinguishable resonances of ^{82}Kr and ^{83}Kr isotopes. The lower resonance absorption cross section of these natural isotopes of Kr gas leads to a weaker resonance dips compared to Xe. The theoretical transmission calculated with fitted thickness parameters for Fe, Kr, Mo and Co shown by the solid line in Fig. 7 still enables identification of areas where Kr gas is present in the pipe, but with a lower accuracy on the measured quantity of that gas.

2. Pressure of gaseous materials

The partial pressures of gaseous substances can be reconstructed if the volume occupied by gaseous material is known, as seen from Equation (5). For a simplified case, when only one element in the sample assembly is in the gaseous form the pressure of the gas can be calculated from equation:

$$P_{Xe,Kr} = \frac{kT}{d_{Xe,Kr} \sum_j \sigma_j(E)A_j} ln \left[\frac{Tr_{solid}(E)}{Tr(E)} \right] \tag{6}$$

where j index indicates different isotopes of these gases, $d_{Xe,Kr}$ is the effective thickness of the gas, $\sigma_j(E)$ and A_j are their attenuation cross section and abundance, respectively. The pressure reconstructed from Equation (6) is most accurate for energies at which the attenuation cross section is the highest, as demonstrated in Fig. 8. Absorption peaks, corresponding to ^{124}Xe, ^{129}Xe and ^{131}Xe isotopes were used for the calculation. Multiple independent measurements are possible using different regions on the detector provided that the pipe internal diameter is accounted for. The parameters for the attenuation by the solid materials (steel pipe) were taken from the fitted spectra of Fig. 6. The transmission spectrum of steel pipe only $Tr_{solid}(E)$ (excluding Xe gas) was first calculated with these parameters (Fig. 8(a)) and then used in Equation (6) for the calculation of xenon pressure within a 0.275 mm-wide regions of the pipe indicated by dashed lines in Fig. 6(g). Same $Tr_{solid}(E)$ can be obtained experimentally for the pipe not filled with the gas. Apparently the accuracy of pressure reconstruction decreases from the center to the edge of the pipe due to the smaller effective thickness of gas encountered by neutrons. Moreover, not entire measured spectrum should be used in the analysis: an accurate reconstruction of pressure value is possible only from the part of the transmission spectrum where attenuation coefficient of gas is relatively high, otherwise both terms $ln \left[\frac{Tr_{solid}(E)}{Tr(E)} \right]$ and $\sigma_j(E)$ in Equation (6) become small leading to a large error. The calibrated attenuation cross
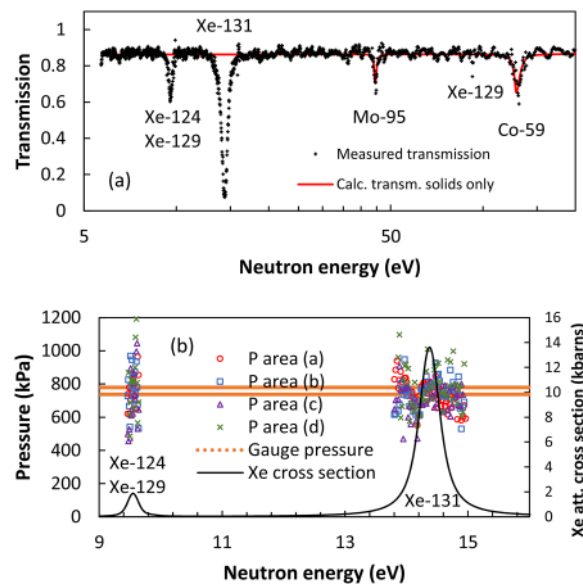

FIG. 8. (a) Measured transmission spectrum $Tr(E)$ and calculated spectrum for solid materials only $Tr_{solid}(E)$ (transmission of steel pipe) for the area (a) of Fig. 6(g). (b) Reconstructed pressure of Xe gas in the pipe (markers), calculated around two resonance energies for the areas (a)-(d) of Fig. 6(g). The value measured with a pressure gauge is shown by the dotted lines bounding the measured value by ±21 kPa. The location of Xe resonances is shown by the sold line representing ^{nat}Xe attenuation cross section.

section of ^{nat}Xe gas shown in Fig. 8(b) exhibits two resonances at ~9.55 eV and ~14.4 eV. The symbols indicate the absolute pressure values reconstructed from Equation (6) for multiple energy values E for the areas (a)-(d) determined in Fig. 6(g). Since the pressure value does not depend on neutron energy a linear fit to these extracted values can be used to reconstruct the pressure in a given region of the steel pipe. The dispersion around the average reconstructed value is higher at ~9.55 eV resonance, which has a lower resonance cross section. The reconstructed pressure values of Xe gas appeared to be 739±98 kPa and 751±154 kPa for 14.4 eV and 9.55 eV resonances, respectively. These values are in a relatively good agreement with the value of 758±21 kPa determined with the help of a pressure gauge. As demonstrated here, the quantification of gases can be performed with some spatial resolution.

Therefore this technique can still be implemented in cases where several secluded sections exist within the sample as partial pressure can be reconstructed within a small area of the image.

The accuracy of the pressure reconstruction can be improved by a multi-parameter fit to the entire spectrum. Under ideal circumstances this would account for each pixel and take into account variations in the pipe thickness. Then the average value of pressure across the entire sample can be taken as a final answer if it is known that sample has no isolated sections. The accuracy of pressure reconstruction can also be improved if a thicker gas volume and/or a higher gas pressure are measured.

C. Element-specific imaging

In addition to quantification of gaseous substances, the quantified maps of elemental composition with ~100 μm spatial resolution can be extracted from the same dataset acquired in energy-resolved neutron imaging experiments. That can be very attractive for the applications where the spatial distribution of gases relative to other elements is important. The amount of material in a small area, which can be extracted by multi-parameter fitting of the theoretical transmission curves into the measured spectra, can be demonstrated for any region of the detector that offers data of adequate statistical quality. In the limiting case this could correspond to an individual pixel. Fitting with dedicated tools, such as SAMMY code[35] or as reported in references[17,22,23] can be implemented for more accurate quantification of the elemental composition and it is a subject of a separate dedicated study.[32] The accuracy of the quantification depends on factors that include; the number of neutrons acquired in each spectrum, the strength of the resonance absorption cross section and the accuracy of fitting. Repeating this analysis for every pixel requires a substantial amount of computational power.

A semi-quantitative analyses of elemental composition can be performed quickly, even during the experiment, for the assessment of the elemental distribution within the sample, as demonstrated in this section by imaging of multiple overlapping materials as in configuration 2 of Fig. 1. The spectrum over the area, shown by a wide rectangle in the image of Fig. 9.a exhibits resonance dips corresponding to all the elements present in the sample, consisting of urania pellets with Gd and W inclusions, all sealed in a steel pipe.

We demonstrate here that an image, specific to a particular element, with contribution of other materials nearly non-existent or at least greatly suppressed can be reconstructed from the data. That is achieved by division of images acquired at the resonance energies of a particular element (e.g. regions 1, 2 and 3 of spectrum shown in Fig. 9(a)) by the images corresponding to the part of spectrum where no resonances are present (region "norm" of spectrum 9.a). Such reconstructed element specific images for ^{238}U, W, Xe and Gd are shown in Figs. 9(b)–9(e). The same type of element-specific images were obtained for the sample configuration 3, shown in Fig. 10. The tungsten wires of varying diameter enclosed within 5 mm urania pellets can be easily visualized even for a wire diameter of 50 μm, as seen in Fig. 10(c), demonstrating the spatial resolution consistent with the pixel size. The voids in and between urania pellets can also be easily visualized from the same data set by the ratio of transmission images acquired in the epithermal range of energies to images of a thermal neutron transmission. These images demonstrate the uniqueness of neutron energy-resolved imaging at epithermal range of energies to provide element-specific (isotope specific) maps of materials (including gaseous ones) which are enclosed or obscured by other materials (including high-Z), opaque to other more conventional imaging techniques.
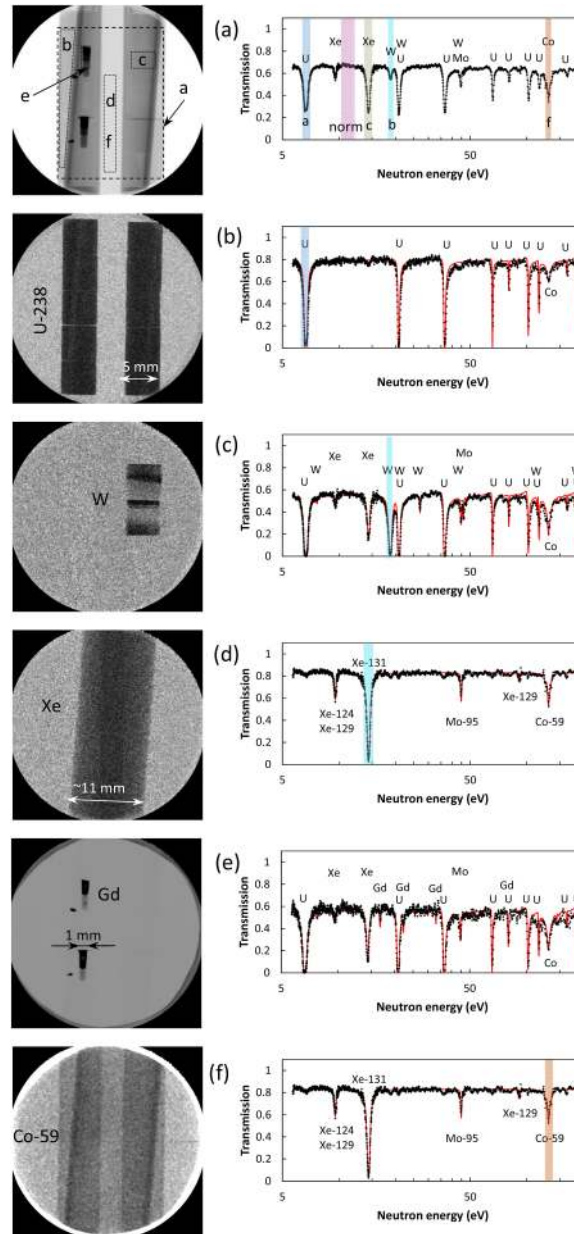
FIG. 9. Element-specific images acquired with samples in configuration 2. (a) Full spectrum (white beam) radiograph and a spectrum obtained in the area indicated by a wide dashed rectangle. The letters in the radiograph indicate the areas for which spectra are extracted in figures (b)-(f). The energy ranges shown by the shaded areas in the spectrum of figure (a) indicate the energy range for the subset of images which were used to reconstruct the element-specific maps (b)-(f), except for the map of Gd, where thermal neutrons were used due to high absorption cross section of Gd. ^{238}U, W, Xe and Gd are imaged separately from other elements despite the fact they were overlapped with each other as well as with steel pipes. Steel pipes are visualized by the resonance of ^{59}Co in image (f), which is normalized by the full spectrum open beam image. Iron itself has non-negligible attenuation in the entire range of measured energies, but does not have resonances.

D. Microstructure of solid crystalline materials

Thermal neutron diffraction has been widely used for the studies of microstructure within various crystalline materials and lately the use of neutron transmission techniques was demonstrated for the same purpose.[4,7–14] The energy resolved neutron imaging reported in this paper covers a broad range of neutron energies, including the thermal and cold neutrons. Therefore not only elemental mapping can be performed from the data acquired in such experiments, but also some microstructure parameters can
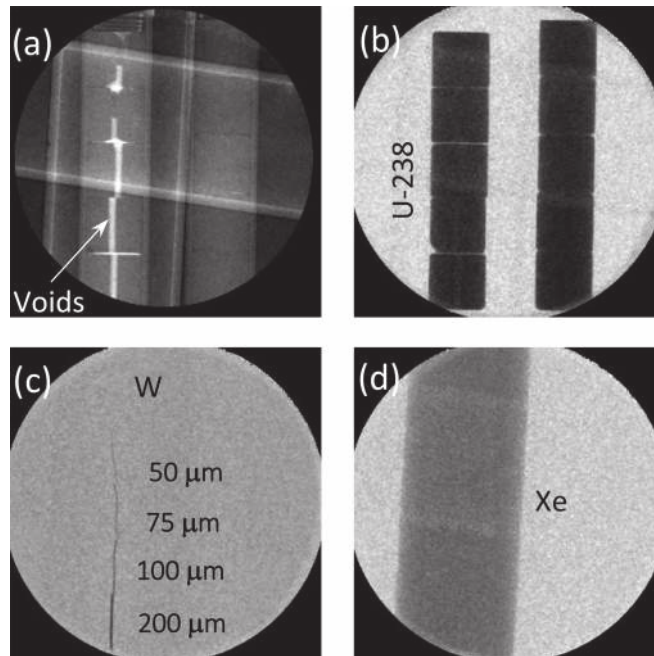
FIG. 10. (a) Image of voids within $^{238}UO_2$ pellets. The contrast is enhanced by normalization of images acquired at the energies of 49 meV to 1.3 eV by images acquired in 4.6 meV to 48 meV range of energies. (b)-(d) Element-specific images of ^{238}U, W and Xe gas, all acquired simultaneously for sample configuration 3. The 50 μm W wire mounted inside of urania pellet is clearly visible, as well as Xe gas encapsulated in steel pipe and obscured by steel, urania and W. The same normalization as in Fig. 9 was used to reconstruct the element-specific images (b)-(d).

be reconstructed at the same time, as demonstrated by all the previous thermal neutron transmission studies. The strain distribution in the cladding of nuclear fuel assembly, for example, can be studied simultaneously with the elemental distribution within the samples. The transmission technique strictly does not allow a quantification of residual stresses. Indeed, in the center region of the pipe neutrons probe the strain in the radial direction, while in the outer region of the pipe hoop strains are measured, with a mixture of both strains in between them. However, such characterization would allow to identify inhomogeneities of the strain between different regions in the axial direction, providing guidance for more localized or destructive examination using other techniques. The transmission spectra of the steel fuel cladding and the steel pipe containing Xe gas shown in Fig. 11 in a wide range of energies, exhibits typical Bragg edges, which can be used for the reconstruction of residual strain. Such analysis is not included in the present paper as no strain was expected in the mockup fuel assemblies used in
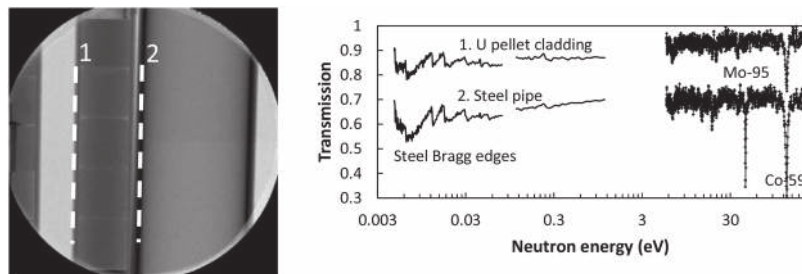

FIG. 11. Full spectrum (white beam) radiograph of sample configuration 1 and a full transmission spectrum of steel cladding and steel pipe measured in the areas indicated by the dashed lines at the edge of the pipe (corresponding to the thickest part of steel seen by neutrons). Typical steel Bragg edges are seen at the thermal neutron energies <100 meV. Some microstructure properties of steel can, in principle, be reconstructed from such spectra (not attempted in the present study due to limited neutron statistics). The cladding steel did not contain as much ^{95}Mo as the steel pipe filled with Xe gas. That difference in transmission spectrum can be used to differentiate the two steels in the image.

our experiment and no sufficient neutron statistics per small area were acquired for the reconstruction of strain.

IV. CONCLUSION

The energy-resolved neutron imaging technique implemented at spallation neutron sources described in this paper enables simultaneous acquisition of neutron transmission spectra within each pixel of data set in a wide range of neutron energies, spanning from epithermal energies to cold neutrons. These spatially-resolved neutron transmission measurements provide a unique possibility to reconstruct the maps of bulk elemental (isotope-specific) composition within samples opaque to other more conventional imaging techniques, based on X-ray of electron interrogation. In addition to previously reported mapping of solids, we demonstrate here that gaseous substances can be imaged with relatively high spatial resolution within the samples consisting of high-Z materials. For elements with relatively high resonance absorption cross section (exceeding $\sim10^3$-10^4 barn) this technique can also be used to quantify the number of gas atoms present in the path of neutrons, which can be converted into gas partial pressure if geometry is known.

A more detailed analysis will be required for the estimation of the sensitivity limit of this approach, i.e. what is the minimum amount of gas molecules or lowest gas pressure which can be reconstructed in such experiments. It will definitely not be as accurate as other more sensitive techniques, such as X-ray or Gamma-ray fluorescence in quantification of isotopic ratios, for example. However neutron energy-resolved imaging is an attractive complementary method for the cases where other interrogation techniques fail due to sample opacity or where quantification with spatial resolution is not possible.

Although the technique described in this paper provides the means to measure gas pressures remotely but with limited resolution and only for relatively high gas pressures or large volumes it is still a very unique method for the studies of substances concealed within high-Z materials, such as interrogation of spent nuclear fuel assemblies, pre-screening of rare samples such as double-sealed containers with lunar materials, cultural heritage objects and others. It can also be used for a remote measurement of gas leaks even in the case of double-sealed containers.

ACKNOWLEDGMENTS

[1] *Neutron Imaging and Applications: A Reference for the Imaging Community*, edited by I. S. Anderson, R. McGreevy, and H. Z. Bilheux (Springer, 2009).

[2] N. Kardjilov, I. Manke, A. Hilger, M. Strobl, and J. Banhart, "Neutron imaging in materials science," Mater. Today **14**, 248 (2011).

[3] E. H. Lehmann, A. Tremsin, C. Grünzweig, and A. Kaestner, "Neutron Imaging – detector options in progress," J. Instrum. **6**, C01050 (2011).

[4] W. Kockelmann, G. Frei, E. H. Lehmann, P. Vontobel, and J. R. Santisteban, "Energy-selective neutron transmission imaging at a pulsed source," Nucl. Instr. Meth. A **578**, 421 (2007).

[5] Y. Kiyanagi, T. Kamiyama, O. Takada, K. Morita, K. Iwase, S. Suzuki, M. Furusaka, F. Hiraga, S. Tomioka, K. Mishima, N. Takenaka, and T. Inod, "Imaging and texture observation of materials by using a pulsed neutron spectroscopic transmission method," Nucl. Instr. Meth. A **600**, 167–169 (2009).

[6] M. Schulz, P. Boni, E. Calzada, M. Muhlbauer, and B. Schillinger, "Energy-dependent neutron imaging with a double crystal monochromator at the ANTARES facility at FRM II," Nucl. Instr. Meth. A **605**, 33 (2009).

[7] S. Vogel, "A rietveld-approach for the analysis of neutron time-of-flight transmission data," Ph.D. thesis, Kiel University, Germany, 2000.

[8] R. R. Dehoff, M. M. Kirka, W. J. Sames, H. Bilheux, A. S. Tremsin, L. E. Lowe, and S. S. Babu, "Site specific control of crystallographic grain orientation through electron beam additive manufacturing," Materials Science and Technology **31**, 931–938 (2015).

[9] F. Malamud and J. R. Santisteban, "Full-pattern analysis of time-of-flight neutron transmission of mosaic crystals," J. Appl. Cryst. **49**, 1 (2016).

[10] A. S. Tremsin, S. Ganguly, S. Meco, G. R. Pardal, T. Shinohara, and W. B. Feller, "Non-destructive studies of dissimilar metal welds by energy resolved neutron imaging," J. Appl. Crystallography **49**, 1130–1140 (2016).

[11] A. Steuwer, J. R. Santisteban, P. J. Withers, L. Edwards, and M. E. Fitzpatrick, "In situ determination of stresses from time-of-flight neutron transmission spectra," J. Appl. Crystallography **36**, 1159–1168 (2003).

[12] H. Sato, T. Sato, Y. Shiota, T. Kamiyama, A. S. Tremsin, M. Ohnuma, and Y. Kiyanagi, "Relation between vickers hardness and bragg-edge broadening in quenched steel rods observed by pulsed neutron transmission imaging," Materials Transactions **56**, 1147–1152 (2015).

[13] A. S. Tremsin, T. Y. Yau, and W. Kockelmann, "Non-destructive examination of loads in regular and self-locking spiralock® threads through energy-resolved neutron imaging," Strain (2016).

[14] R. Woracek, D. Penumadu, N. Kardjilov, A. Hilger, M. Boin, J. Banhart, and I. Manke, "3D mapping of crystallographic phase distribution using energy-selective neutron tomography," Advanced Materials **26**, 4069 (2014).

[15] R. A. Schrack, J. W. Behrens, R. G. Johnson, and C. D. Bowman, "*Resonance Neutron Radiography*," J. P. Barton and P. von de Hardt (eds.), Neutron Radiography, 495–502. Copyright © 1983 ECSC, EEC, EAEC, Brussels and Luxembourg.

[16] G. Gorinia, E. Perelli-Cippo, M. Tardocchi, C. Andreani, A. D'Angelo, A. Pietropaolo, R. Senesi, S. Imberti, A. Bracco, E. Previtali, G. Pessina, N. J. Rhodes, and E. M. Schooneveld, "The resonant detector and its application to epithermal neutron spectroscopy," Nucl. Instr. Methods Phys. Res. A **529**, 293 (2004).

[17] P. Schillebeeckx, A. Borella, F. Emiliani, G. Gorini, W. Kockelmann, S. Kopecky, C. Lampoudis, M. Moxon, E. P. Cippo, H. Postma, N. J. Rhodes, E. M. Schooneveld, and C. Van Beveren, "Neutron resonance spectroscopy for the characterization of materials and objects," J. Instrumentation **7**, C03009 (2012).

[18] A. S. Tremsin, S. C. Vogel, M. Mocko, M. A. M. Bourke, V. Yuan, R. O. Nelson, D. W. Brown, and W. B. Feller, "Non-destructive studies of fuel rodlets by neutron resonance absorption radiography and thermal neutron radiography," J. of Nucl. Materials **440**, 633 (2013).

[19] A. S. Tremsin, T. Shinohara, T. Kai, M. Ooi, T. Kamiyama, Y. Kiyanagi, Y. Shiota, J. B. McPhate, J. V. Vallerga, O. H. W. Siegmund, and W. B. Feller, "Neutron resonance transmission spectroscopy with high spatial and energy resolution at J-PARC pulsed neutron source," Nucl. Instr. Meth. A **746**, 47–58 (2014).

[20] G. Festa, E. P. Cippo, D. D. Martino, R. Cattaneo, R. Senesi, C. Andreani, E. Schooneveld, W. Kockelmann, N. Rhodes, A. Scherillo, P. Kudejova, K. Biro, K. Duzs, Z. Hajnal, and G. Gorinia, "Neutron resonance transmission imaging for 3D elemental mapping at the ISIS spallation neutron source," J. Anal. Atom. Spectrom. **30**, 745 (2015).

[21] H. Hasemi, M. Harada, T. Kai, T. Shinohara, M. Ooi, H. Sato, K. Kino, M. Segawa, T. Kamiyama, and Y. Kiyanagi, "Evaluation of nuclide density by neutron resonance transmission at the NOBORU instrument in J-PARC/MLF," Nucl. Instr. Meth. Phys. Res. A **773**, 137 (2015).

[22] H. J. Stone, M. G. Tucker, F. M. Meducin, M. T. Dove, S. A. T. Redfern, Y. Le Godec, and W. G. Marshall, "Temperature measurement in a Paris-Edinburgh cell by neutron resonance spectroscopy," J. Appl. Phys. **98**, 064905 (2005).

[23] V. W. Yuan, J. D. Bowman, D. J. Funk, G. L. Morgan *et al.*, "Shock temperature measurement using neutron resonance spectroscopy," Phys. Rev. Let. **94**, 125504 (2005).

[24] A. S. Tremsin, W. Kockelmann, D. E. Pooley, and W. B. Feller, "Spatially resolved remote measurement of temperature by neutron resonance absorption," Nucl. Instr. Meth. A **803**, 15–23 (2015).

[25] V. Wagner, H. Friedrich, and P. Wille, "Performance of a high- tech neutron velocity selector," Phys. B: Cond. Matter **938**, 180–181 (1992).

[26] W. Treimer, M. Strobl, N. Kardjilov, A. Hilger, and I. Manke, "A wave length tunable device for neutron radiography and tomography," Appl. Phys. Lett. **89**, 203504 (2006).

[27] Evaluated Nuclear Data File (ENDF) for Available at: https://www-nds.iaea.org/exfor/endf.htm (Accessed: October 2016).

[28] A. S. Tremsin, J. V. Vallerga, J. B. McPhate, O. H. W. Siegmund, and R. Raffanti, "High resolution photon counting with MCP-timepix quad parallel readout operating at > 1KHz frame rates," IEEE Trans. Nucl. Sci. **60**, 578–585 (2013).

[29] A. S. Tremsin, J. V. Vallerga, J. B. McPhate, and O. H. W. Siegmund, "Optimization of high count rate event counting detector with microchannel plates and quad timepix readout," Nucl Instr. Meth. A **787**, 20–25 (2015).

[30] M. Mocko, G. Muhrer, Ch. T. Kelsey, M. A. Duran, and F. Tovesson, "Experimental measurement of the neutron time-emission spectra at the manuel Lujan Jr. neutron scattering center," Nucl. Instr. Meth. A **632**, 101 (2011).

[31] www.novascientific.com.

[32] A. S. Losko, S. C. Vogel, A. S. Tremsin, K. J. McClellan, M. A. Bourke, D. D. Byler, M. Mocko, P. Hosemann, and H. Nakotte, "Imaging of nuclear fuel using time-of-flight neutrons," to be submitted.

[33] M. Grosse, M. van den Berg, C. Goulet, E. Lehmann, and B. Schillinger, "In-situ neutron radiography investigations of hydrogen diffusion and absorption in zirconium alloys," Nucl. Instr. Meth. A **651**, 253–257 (2011).

[34] S. Borries, O. Metz, P. K. Pranzas, J. M. Bellosta von Colbe, T. Bücherl, M. Dornheim, T. Klassen, and A. Schreyer, "Optimization and comprehensive characterization of metal hydride based hydrogen storage systems using in-situ neutron radiography," J. Power Sources **328**, 567–577 (2016).

[35] N. M. Larson, "Introduction to the theory and analysis of resolved (and unresolved) neutron resonances via SAMMY", Edited by N. Paver, M. Herman, and A. Gandini, *Nuclear Reaction Data and Nuclear Reactors: Physics, Design and Safety*, Ns 1 and 2, Book Series: ICTP LECTURE NOTES SERIES, Volume: 5, 1–46, 2001.